Article

Reconstruction of a segment of the UNESCO World Heritage Hadrian's Villa tunnel network by integrated GPR, magnetic–paleomagnetic, and electric resistivity prospections

Annalisa Ghezzi[1,*], Antonio Schettino[1], Pietro Paolo Pierantoni[1], Lawrence Conyers[2], Luca Tassi[1], Luigi Vigliotti[3], Erwin Schettino[4], Milena Melfi[5], Maria Elena Gorrini[6] and Paolo Boila[7]

[1] University of Camerino – School of Science and Technology, Camerino, Italy; E-Mails: antonio.schettino@unicam.it (A.S.); pietropaolo.pierantoni@unicam.it (P.P.P.); luca.tassi@unicam.it (L.T.)
[2] Department of Anthropology, University of Denver, Denver, CO 80210, USA; E-Mail: lconyers@du.edu (L.C.)
[3] Istituto di Scienze Marine , CNR, Bologna, Italy; E-Mail: luigi.vigliotti@bo.ismar.cnr.it (L.V.)
[4] Instituto Andaluz de Ciencias de la Tierra, CSIC – Universidad de Granada, Spain; E-Mail: eschettino@correo.ugr.es (E.S.)
[5] Faculty of Classics - University of Oxford, Oxford, UK; E-Mail: milena.melfi@classics.ox.ac.uk (M.M.)
[6] Dipartimento di Studi Umanistici, Università degli studi di Pavia, Pavia, Italy; E-Mail: mariaelena.gorrini@unipv.it (M.E.G.)
[7] Idrogeotec S.N.C. - Perugia - Italy; E-Mail: idrogeotec@tin.it (P.B.)

* Correspondence: annalisa.ghezzi@unicam.it (A.G.); Tel.: +39–0737–402641

Abstract: The UNESCO World Heritage Hadrian's Villa lies over the Colli Albani volcanic district near Rome. Magnetic, paleomagnetic, radar, and electric resistivity surveys were performed in the Plutonium–Inferi sector to detect buried buildings and outline a segment of the underground system of tunnels that link different zones of the villa. In particular, a paleomagnetic analysis of the bedrock unit allowed to accomplish an accurate geomagnetic field modelling and characterize the archaeological sources of the magnetic field anomalies. We used a computer–assisted forward modelling procedure to generate a structural model of the sources of the observed anomalies. The intrinsic ambiguity of the magnetic field modelling was reduced with the support of ground penetrating radar amplitude slices and an analysis of radar and electric resistivity profiles. The bedrock lithology in this area is an ignimbrite tuff characterized by abundant iron oxides. The high–amplitude magnetic anomalies observed in the Plutonium–Inferi area are due to strong bedrock remnant magnetization and susceptibility contrasts between topsoil infill of cavities and the surrounding tuff. The resulting magnetization model of the Plutonium–Inferi complex shows that the observed anomalies are mostly due to the presence of tunnels, skylights and a system of ditches excavated in the tuff.

Keywords: Archaeological geophysics; magnetic methods; ground penetrating radar; tunnel detection; data integration.

1. Introduction

Hadrian's Villa is a UNESCO World Heritage site near Rome (Figure 1). It was built starting from 117–118 A.D. as one of the residences of the Roman Emperor Hadrian. Its location was chosen for its scenic location, proximity to Rome, and the presence of four aqueducts directed to Rome.

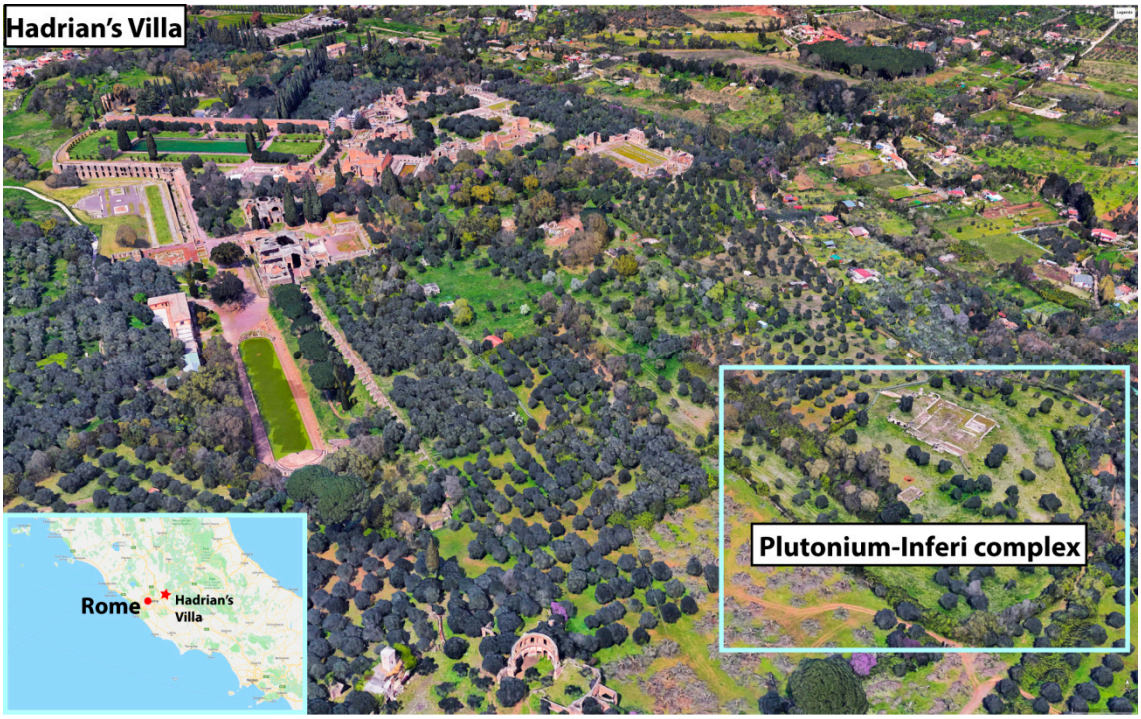

Figure 1. Hadrian's Villa Archaeological Site.

The villa lies over the Quaternary Colli Albani volcanic district, a ~600 ka to present undersaturated K–rich magmatic province that is part of the ~250 km long peri–Thyrrhenian volcanic belt [1]. The geological framework of this site consists of a complex volcano–sedimentary succession made of ignimbrite sheets interposed with fall deposits and lava flows [2]. Irregularity in geometry and thickness, as well as lateral facies variations and heterogeneous alteration of the stratigraphic units are related to the paleotopographic control on the transport and depositional mechanisms of the volcanic products. The outcropping lithology at Hadrian's Villa consists of the Pozzolanelle ignimbrite, the upper depositional unit of the Villa Senni eruption unit, which represents the youngest (355 ka) mafic caldera–forming eruption of the Colli Albani [3,4]. The Pozzolanelle unit is a chaotic, ignimbritic tuff massive deposit, ranging in thickness from < 2 to 40 m, characterized by an ash matrix support texture abundant with phenocrystals (leucite, clinopyroxene, and biotite), holocrystalline xenoliths, and reddish vesicular scoria clasts [5] (Figure 2).

The archaeological structures of this large villa include many monumental buildings and an important underground network of tunnels that was created to link different parts of the complex and, possibly, for the transport of supplies [6]. Nowadays only a small part of this network can be travelled by non–speleologists. The first systematic description of Hadrian's Villa was carried out by Pirro Ligorio in the XVI [7]. Ligorio was the first to draw a complete map of the site and to attempt an identification of the function of any specific feature of the villa by assigning names to its various parts. One century later, Contini drew a more accurate map of the system of tunnels that run beneath the villa on the basis of the earlier study by Ligorio [8]. His map was accepted without substantial modifications by all the following draughtsmen, including Piranesi ([6] and references therein). However, an important contribute to the characterization of the architectural elements of the villa was provided at the beginning of the XIX by [9], who accurately described and recorded both exposed structures and the accessible subterranean features (already mapped by earlier authors). More recently, an accurate topographic survey of the network of tunnels was performed by [6] (Figure 3), who divided the underground features in four categories according to their functionality. The first category includes brick dressed cryptoportica and ambulacra. The second category comprises underground tunnels for use of both pedestrians and carts, occasionally interrupted by open–air segments. The third category includes underground pedestrian passages linking different buildings of the villa, smaller in size than those of the former category. Finally, the last category consists of a heterogeneous set of basements and underground rooms with different purposes.

Peer-reviewed version available at Remote Sens. 2019, 11, 1739; doi:10.3390/rs11151739

Figure 2. Stratigraphic section of the substratum of Hadrian's Villa. The picture was taken along the Via Tiburtina close to the highway entrance to Tivoli.

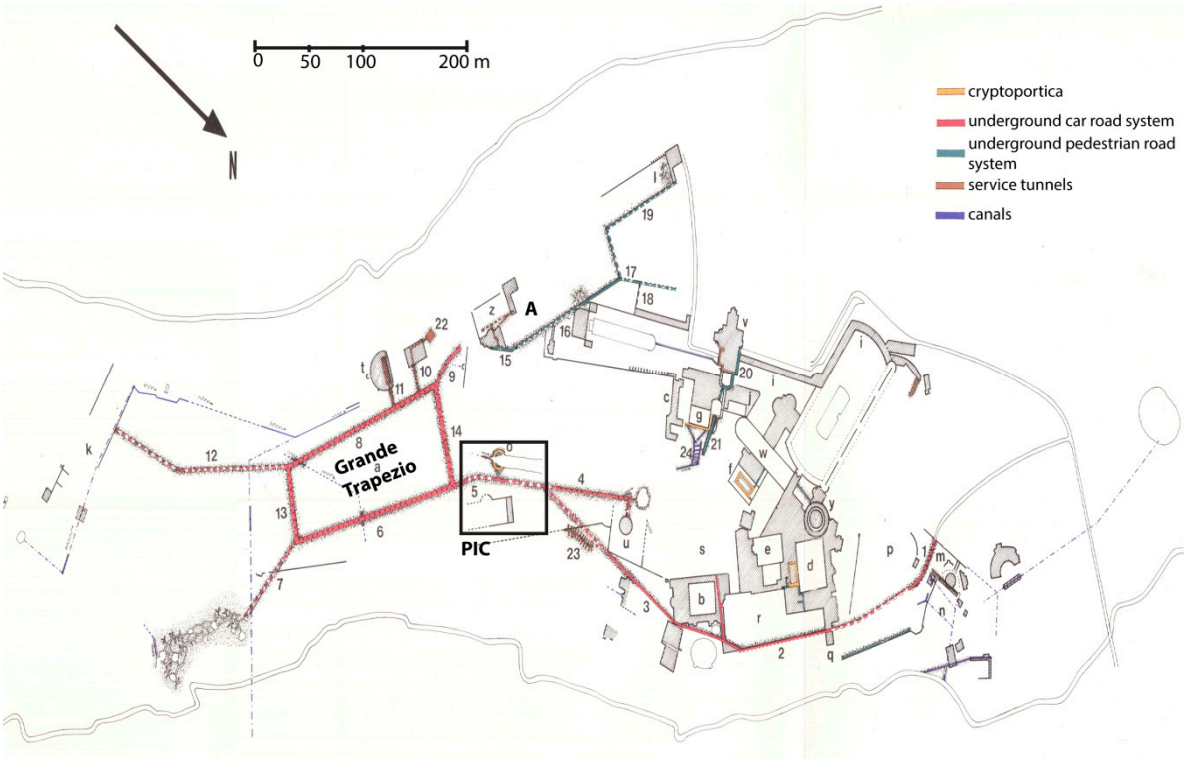

Figure 3. Hadrian's Villa general plan (modified from [6]). PIC = Plutonium–Inferi complex; A = Accademia.

Despite the paramount archaeological importance of Hadrian's Villa, there is a very scarce record of published geophysical investigations at this site. Franceschini and Marras [10] applied for the first time electric resistivity methods to reconstruct the layout of the subterranean tunnels in the area of the Accademia (Figure 3). Their results substantially confirmed the map of Piranesi for this

sector of the villa. A ground penetrating radar (GPR) survey of the area around the Plutonium–Inferi complex (Figure 1) was undertaken in 2016 by a team of the British School at Rome [11] to facilitate successive excavations in the context of a joint project of the universities of Oxford and Pavia [12]. The radar survey was performed using a 400 MHz antenna, which did not allow sufficient penetration for investigating the system of tunnels that had been dug in the tuff units underlying the Plutonium–Inferi area. The maximum penetration depth of this survey was ~100 cm, thereby the resulting amplitude maps only showed archaeological features buried in the topsoil, and not the cavities in the underlying rock formation. To date, the most used geophysical technique at Hadrian's Villa has probably been the laser scanner (an interesting example can be found in [13]). Finally, it is worth mentioning the sophisticated surveying techniques (probes and robots) used in recent years by the Centro Ricerche Speleo Archeologiche of Rome, which explored a segment of the underground road system known as the "Strada Carrabile" [14].

We performed an integrated geophysical survey at one of the least known sectors of Hadrian's Villa, the Inferi–Plutonium complex (Figure 1), with the objective of reconstructing a segment of the underground tunnel network in this area (Figure 4).

Figure 4. Tunnels in the Plutonium – Inferi complex.

The buildings in the Inferi–Plutonium area have been generally understood as related to the belief of an after–life existence and the cult of death [15]. According to this hypothesis, that dates back to the first explorations by Pirro Ligorio, the Inferi, a large ditch dug in the tuff, would represent the River Styx and the entrance to the Underworld, while the Plutonium would be a temple devoted to Pluto, king of the Underworld. The present study aims at detecting cavities in the tuff units by combining several sources of data, obtained from different geophysical methods: electric resistivity, magnetometry, GPR, paleomagnetism, and aerial photogrammetry. The whole area was covered by the GPR survey, but because of the presence of fences or iron scraps, the magnetic data were collected only in the central and western portion of the complex.

The strong magnetic susceptibility χ and natural remnant magnetization (NRM) of the tuff units on which Hadrian's Villa was built has amplified the contrast with the buried structures and the cavities in the substratum, so that the corresponding magnetic anomalies reach amplitudes up to ~2200 nT. In a sense, the bedrock geology of this site is a unique example of a natural "amplifier" of magnetic anomalies associated with archaeological features. Consequently, we used the magnetic data set as the primary source for reconstructing the layout of the tunnel network by using a technique of forward modelling, but the whole procedure and the results were constrained and assessed, respectively, by the other sources of data. In particular, the integration with GPR data allowed to extend the reconstruction beyond the area surveyed with magnetic methods, while both amplitude slices and individual radar profiles were used to constrain the geometry of the

magnetization model. In the next sections, we first discuss the various techniques used for the data acquisition and processing, then we show how the different sources of data were integrated in order to reconstruct the topology of the tunnel network underneath the Plutonium–Inferi area. Our results confirm the presence of tunnels whose existence was already known, but also reveal the existence of additional underground tunnels and of a system of ditches dug at the top of the tuff, which probably served as irrigation channels.

2. Methods

Initially, magnetic, radar, and electric resistivity surveys performed in 2017–2018 had the primary objective of assessing potential security issues during the excavations around the Plutonium–Inferi complex. In addition, paleomagnetic and precise topographic data were acquired in view of the creation of a reliable magnetization model of the buried structures and cavities. Below we describe in detail the acquisition and processing methods for each of the geophysical techniques used in this survey.

2.1. GPR Data Acquisition and Processing

GPR data were acquired using a GSSI SIR 4000 system equipped with a 200 MHz antenna, which in principle should have allowed sufficient penetration for investigating the system of tunnels that had been dug in the tuff units underlying the Plutonium–Inferi complex. However, the soil of this area includes abundant clays that formed by weathering of the volcanic substratum. In moist conditions, these clays display strong electric conductivity and attenuation, thereby the maximum depth of penetration did not generally exceed 2.5 m. GPR data were acquired using the following basic parameters:

- Survey mode = Distance mode (with odometer)
- Scans/m = 50
- Samples/scan = 1024
- Range = 300 ns
- Bits/sample = 32
- Line spacing = 0.5 m
- Antenna = GSSI 5106, 200 MHz

To improve the coupling with the ground, the survey lines were travelled using three operators, one at the console and two who drove the large 5106 antenna along the tracklines (Figure 5). Other people were responsible for the setup of the survey geometry, for the GPS positioning, and for the deployment of metric tapes. A local reference frame was established, in order to combine GPR data coming from different areas. We divided the survey region in 13 areas (Figure 6) of variable geometry. In all cases, the survey lines were travelled in bi–directional mode and the local coordinates of the end points were recorded by an operator directly in the field. A set of 14 reference points was established, with assigned local coordinates (ξ_i,ψ_i) and known geographic coordinates (x_i,y_i) obtained by GPS measurements and expressed in the UTM 33 reference frame. A computer algorithm then calculated the best–fitting rigid transformation from local coordinates to UTM by weighted least squares minimization of corner location errors relative to the measured GPS locations. The best–fitting orientation of the local reference frame relative to the UTM datum is illustrated in Figura 5, along with the GPS reference points. In all cases, the misfit between reference point locations and best–fitting UTM coordinates resulted to be less than 1.5 m. The resulting data set underwent the following basic processing steps:

- Band pass filtering (~100 – 300 MHz)
- Background removal
- Migration
- Creation of amplitude slices

Peer-reviewed version available at Remote Sens. 2019, 11, 1739; doi:10.3390/rs11151739

- Normalization
- Equalization
- Knitting

Figure 5. GPR system used to investigate the area and arrangement of operators.

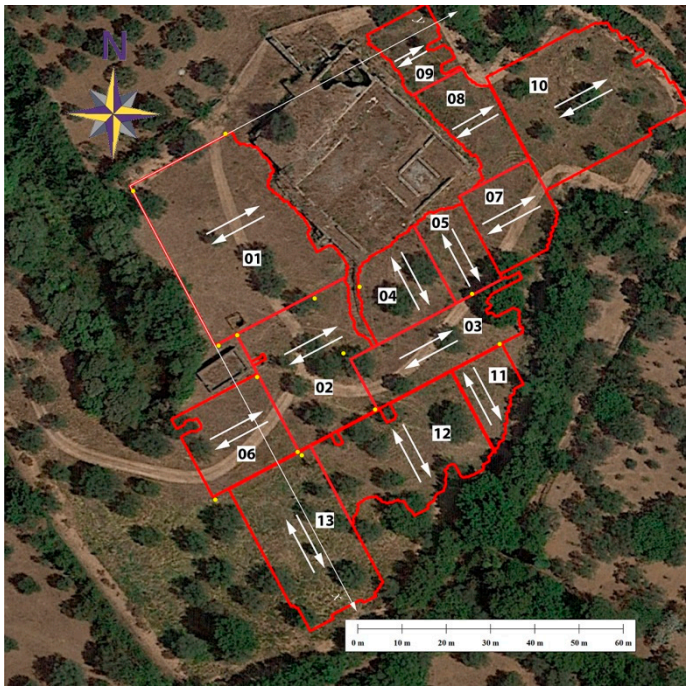

Figure 6. System of 14 GPS points used to define the local reference frame (yellow dots) and GPR survey areas (red lines). The direction of the survey lines is indicated by the white arrows. The coordinate axes (x,y) show the best–fitting reference frame through the assigned GPS points.

To perform the data migration, we searched and fit reliable hyperbolae for each area. Then, laterally homogeneous velocity models were built subdividing the substratum into horizontal layers, different for each area. The average velocity, $\langle v \rangle$, and relative dielectric permittivity, $\langle \varepsilon \rangle$, of each area of Figure 6 is listed in Table 1. These parameters were calculated over a reference two–way travel time (TWTT) interval T = 100 ns starting from the pairs (T_k,v_k) provided by the velocity

195 analysis, T_k and v_k being the TWTT to the bottom of layer k and the corresponding velocity through
196 the same layer, respectively:

197 $$\langle v \rangle = \frac{1}{T} \sum_k v_k \left(T_k - T_{k-1} \right) \quad (1)$$

198 $$\langle \varepsilon \rangle = \frac{c^2}{\langle v \rangle^2} \quad (2)$$

199
200 where c = 30 cm ns^{-1} is the speed of light.
201

Table 1. Average velocity (in cm ns^{-1}) and dielectric constant of the 13 areas of Figure 6

	01	*02*	*03*	*04*	*05*	*06*	*07*	*08*	*09*	*10*	*11*	*12*	*13*
<v>	6.7	9.3	6.6	5.6	8.2	5.0	7.2	4.4	6.3	6.5	7.0	6.7	7.0
<ε>	20.1	10.5	20.8	28.6	13.5	35.8	17.2	45.9	22.5	21.5	18.3	19.9	18.4

202
203 At the next step, 30 cm thick amplitude slices were generated for all the 13 areas, with a 50%
204 overlap between successive slices. From this data set, we chose four meaningful time slices that were
205 representative of shallow, intermediate, and deep-burial depths. These slices were normalized to
206 reduce amplitude differences associated with diverse conditions of the ground. To obtain a mosaic
207 of the 13 areas at each depth, the knitting procedure of the amplitude slices required an equalization
208 step to ensure continuity along the edges of adjacent areas.

209 *2.2. Magnetic Field Intensity Acquisition & Processing*

210 Total field magnetic intensities were collected using a Geometrics G–858 caesium vapor
211 magnetometer. The whole survey area was divided in 10 rectangles having variable dimensions,
212 which were assembled at the end of the processing in the UTM 33N reference frame (Figure 7).
213

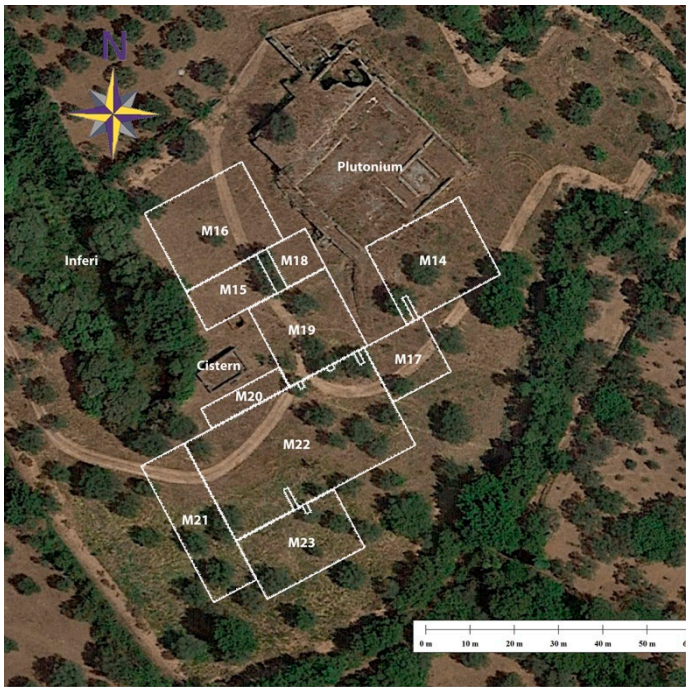

214
215 **Figure 7**. Area covered by the magnetic survey.
216
217 The magnetic data were acquired at 10 Hz frequency (corresponding to an average 11 cm
218 distance between successive readings) along bi–directional survey lines equally spaced 0.5 m. All the
219 total field measurements were performed in solar–quiet conditions, with *Kp* index not exceeding 2

and the data underwent standard pre–processing consisting into despiking and decorrugation procedures. Then, the total field data of each area were decorrugated and combined into a mosaic through an equalization and knitting procedure that ensured continuity along the edges of adjacent areas.

2.3. Paleomagnetic Acquisition & Processing

We sampled 13 cores from the Pozzolanelle unit by using a portable drill. The cores were oriented using a magnetic compass. The sampling was integrated by soil specimens of the substratum in the survey area. The measurements were carried out in the paleomagnetic laboratory of ISMAR–CNR in Bologna. The NRM of the tuff was acquired by these rocks at the time of their deposition and cooling. Therefore, it is an expression of the Earth's magnetic field direction at that time. The induced magnetization of the tuff and soil units depends from their magnetic susceptibility and is directed as the Earth's magnetic field at survey time in the Plutonium–Inferi area. Both the tuff NRM and the magnetic susceptibility of the tuff and soil units represent fundamental quantities that will be used in the subsequent magnetic field modelling procedure.

To determine the magnetic minerals that are responsible for the tuff remnant and induced magnetization components, we applied a Mössbauer spectroscopy technique. This is a powerful method that can be used for the identification of iron–bearing minerals when the magnetic properties of the material are due to a mixture of ferromagnetic minerals. In particular, this technique is very useful when the sample contains minerals with similar magnetic properties, not easily distinguishable using traditional rock magnetic methods, or when weakly magnetic minerals like hematite are mixed with minerals characterized by stronger magnetization, for example magnetite [16]. The absorption spectrum of the Pozzolanelle ignimbrite is shown in Figure 8. The fit to these data is dominated by three strong paramagnetic doublets, but also includes a broad central singlet indicative of the presence of small grains of superparamagnetic iron oxides above their blocking temperature. Finally, the observed spectrum shows four weaker ferromagnetic sextets. The Mössbauer parameters of the doublets are characteristic of Fe^{+3} or Fe^{+2} in octahedral coordination, as it is often observed in the spectrum of biotites, but much more likely arise from the presence of superparamagnetic iron oxyhydroxides such as goethite or ferrihydrite, which are common alteration products in volcanic rocks. These components account for 64% of the spectral area, while another 13% is represented by the superparamagnetic iron oxides. The remaining four ferromagnetic components suggest the presence of maghemite (9%), non–stoichiometric magnetite (7%), and possibly superparamagnetic hematite just below the blocking temperature (8%). Although the interpretation of the latter component is only a tenable hypothesis, it is supported by the large amount of hematite visible on the sample (see Figure 2) and by a preliminary X–ray diffraction analysis performed on the specimen.

In order to obtain the characteristic remnant magnetization (ChRM) of the rock unit, a stepwise alternating field (AF) demagnetization process was applied to the collected samples. The bulk volume susceptibility χ was measured using a Bartington MS2 susceptibility meter and the results were used to calculate the induced magnetization. The rock exhibits a single component of magnetization with only a minor viscous magnetization easily removed after 5 mT of AF field (Figure 9a).

The results listed in Table 2 show that these rocks have strong NRM and a relevant induced magnetization, in agreement with the results of Mössbauer spectroscopy. From these data, we obtain an average volume magnetic susceptibility $\chi = 18126.92 \times 10^{-6}$ SI units. Therefore, assuming a reference field vector F with intensity $F = 46{,}489.2$ nT and direction ($D_0 = 3.14°$, $I_0 = 58.16°$) on Feb 9th 2018 at 41.937567° N, 12.779273° E, it results a mean induced magnetization $M_I = (\chi/\mu_0)F = 0.67$ A m^{-1}. The average NRM intensity results to be $M_R = 4.82$ A m^{-1} (13 specimens mean) with a mean direction: ($D = 4.1°$,$I = 72.8°$) (10 samples average), the statistical parameters k and α_{95} being respectively: k =141.3 and $\alpha_{95} = 4.1°$ (Figure 9b). Taking into account of the rapid deposition and cooling of the pyroclastic flow, this paleomagnetic direction can be considered as representative of the geomagnetic field at the time of deposition of the Pozzolanelle unit.

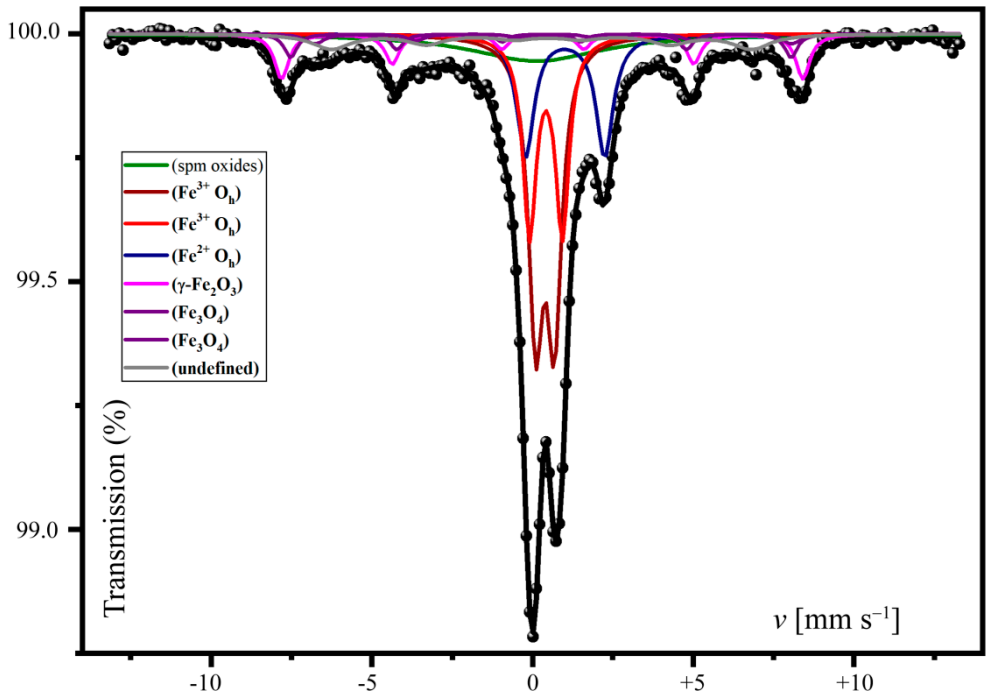

Figure 8. Room temperature ^{57}Fe Mössbauer spectrum of a Pozzolanelle unit specimen. Dots are original data points, black line is the best fitting envelope of the eight spectral components.

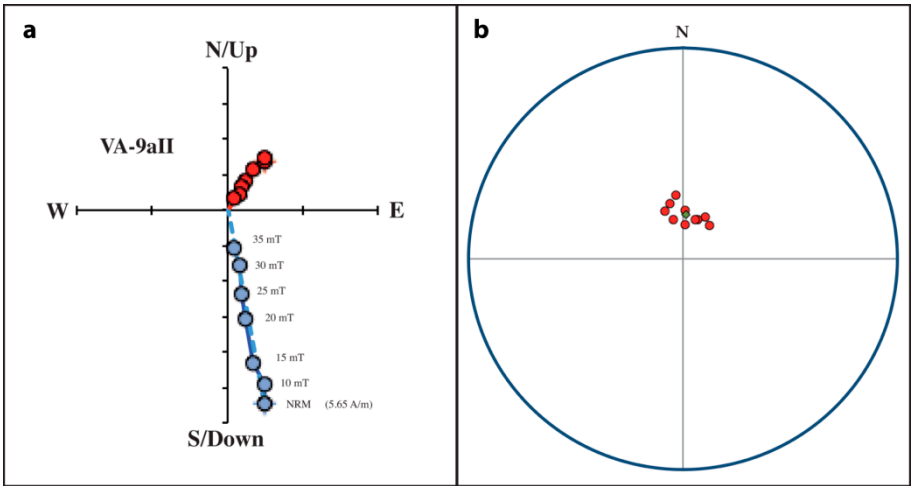

Figure 9. (**a**) AF demagnetization plot; (**b**) Paleomagnetic directions (red dots) with resulting mean (green dot).

Table 2. Results of palaeomagnetic analysis

Sample Id.	D_{PCA}	I_{PCA}	*MAD*	*NRM*	χ	*Q*
VA–4	346.72	74.31	0.88	4.58	18820	6.98
VA–5	2.63	71.10	1.06	4.71	19170	7.05
VA–6aI	27.87	71.73	0.77	4.81	18720	7.38
VA–6aII	38.54	73.77	0.98	5.05	18850	7.68
VA–7aI	347.26	68.20	0.68	4.95	17140	8.29
VA–7aII	353.76	65.32	0.48	5.30	19410	7.83
VA–7aIII	19.76	73.96	0.62	4.84	18360	7.56
VA–8	339.25	70.30	1.29	5.00	18250	7.86
VA–9aII	16.47	74.10	0.63	5.65	18240	8.88
VA–9aI	2.97	76.88	1.10	4.24	14980	8.12

Table 2. Continued

Sample Id.	D_{PCA}	I_{PCA}	*MAD*	*NRM*	χ	*Q*
VA–1				4.07	14800	7.90
VA–2				5.04	22290	6.49
VA–3	29.59	70.48		4.42	16620	7.63

D_{PCA} = NRM declination from principal components analysis [°deg]

I_{PCA} = NRM inclination from principal components analysis [°deg]

MAD = Maximum angular deviation from mean [°deg]

NRM = Remnant magnetization intensity [A m^{-1}]

χ = Magnetic susceptibility [$\times 10^{-6}$]

Q = Koenigsberger ratio

2.4. Electric Resistivity Acquisition & Processing

Electrical resistivity data were acquired using a Geopulse Tigre 128 resistivity meter. The acquisition parameters were set to optimize input current, shape of the current signal input, number of averaged potential readings, and sampling time. This instrument is able to automatically cancel the spontaneous potentials that are eventually generated in the ground and that, in the case of small drops in potential during the measurements, would have been one of the major sources of noise. Before carrying out the measurements, a control test was carried out on the value of the contact resistance between the electrodes and the ground, accepting a resistance value lower than 2000 Ω. We performed ten resistivity acquisitions using 32 electrode spreads. Eight 2D geoelectric profiles out of ten were created using a Wenner–α geometry and 1 m electrode separation, while the remaining two profiles were acquired using a dipole–dipole configuration with 2 m electrode separation. The former array is relatively sensitive to vertical changes in subsurface resistivity below the center of the array and less sensitive to horizontal changes in the subsurface resistivity. The advantage is that a smaller amount of acquisitions is necessary to build a pseudosection. For each profile, the repetition time interval of the square sampling wave was set to 2.8 s, while the number of averaged readings for the estimate of the resistivity was set to 4.

The resulting data set was processed using the software Res2DInv (Geotomo Software), and a search criterion based on the minimum data heterogeneity [17]. In the initial pre–inversion step, we analyzed the data quality of each electric resistivity profile through a test inversion and displayed the resulting root mean square (rms) errors. The subsequent inversion step adopted a strategy based on a 10% increase in the thickness of the layers as the depth increased.

2.5. Aerial Photogrammetry

We used unmanned aerial vehicle (UAV) photogrammetry to create a digital terrain model (DEM) of the Plutonium–Inferi complex (Figure 10) according to the *Structure from Motion* technique. The UAV was a DJI Phantom 4 equipped with an RGB visible light camera, flying at 40 m altitude at ~4 m/s speed. A GPS supported by regional network was used for georeferencing a set of ground control points and scale the aerial photogrammetric survey. The bare–Earth extraction from the DSM was accomplished using the software Photoscan and a point clouds segmentation and classification algorithm. The final DEM was created using the software Thopos (Studio Tecnico Guerra) and covered an area of 30230 m^2 with a pixel size of 0.0456×0.0456 m^2.

Peer-reviewed version available at Remote Sens. 2019, 11, 1739; doi:10.3390/rs11151739

Figure 10. UAV orthophoto of the study area (Plutonium–Inferi complex).

3. Results

We compiled four depth slices, corresponding to the intervals: 45–74 cm, 120–146 cm, 162–187 cm, and 238–262 cm. They are shown in Figure 11. In these maps, the presence of reflectors is indicated by brown colours while their absence is shown in green or blue. The colour intensity is always proportional to the corresponding reflection amplitude. However, it is worth noting that the nature of the reflectors cannot be established by the mere visual inspection of these depth slices. It can be only determined after an analysis of individual radar profiles. The interpretation of amplitude slices is complicated by the fact that structures (and associated reflectors) that are inclined with respect to the Earth surface may be subdivided between different slices and slightly displaced with respect to each other. Excluding long reflectors associated with the contact between stratigraphic units, in general strong localized reflections are produced by: 1. cavities, 2. water–saturated soil, 3. walls and other building remains, 4. modern public utilities, and 5. modern artifacts [18]. However, significant reflections may also be locally associated with partial decoupling of the antenna (for example, as a consequence of a ground surface irregularity), scatterers (e.g., stones), and nearby metals (e.g., fences). All the radar profiles in the data sets 01 through 13 (Figure 6) were analyzed individually to give a precise characterization of the sources of each relevant feature detected on the amplitude slices.

An interesting feature of the 45–74 cm depth slice (Figure 11a) is represented by linear regions characterized by the lack of reflections. An analysis of profiles through these regions shows that they correspond to ditches excavated at the top of the tuff layer, according to the conceptual model shown at the bottom of Figure 11a. This interpretation is in agreement with the 120–146 cm slice (Figure 11b), which shows the base of the ditches as linear reflectors.

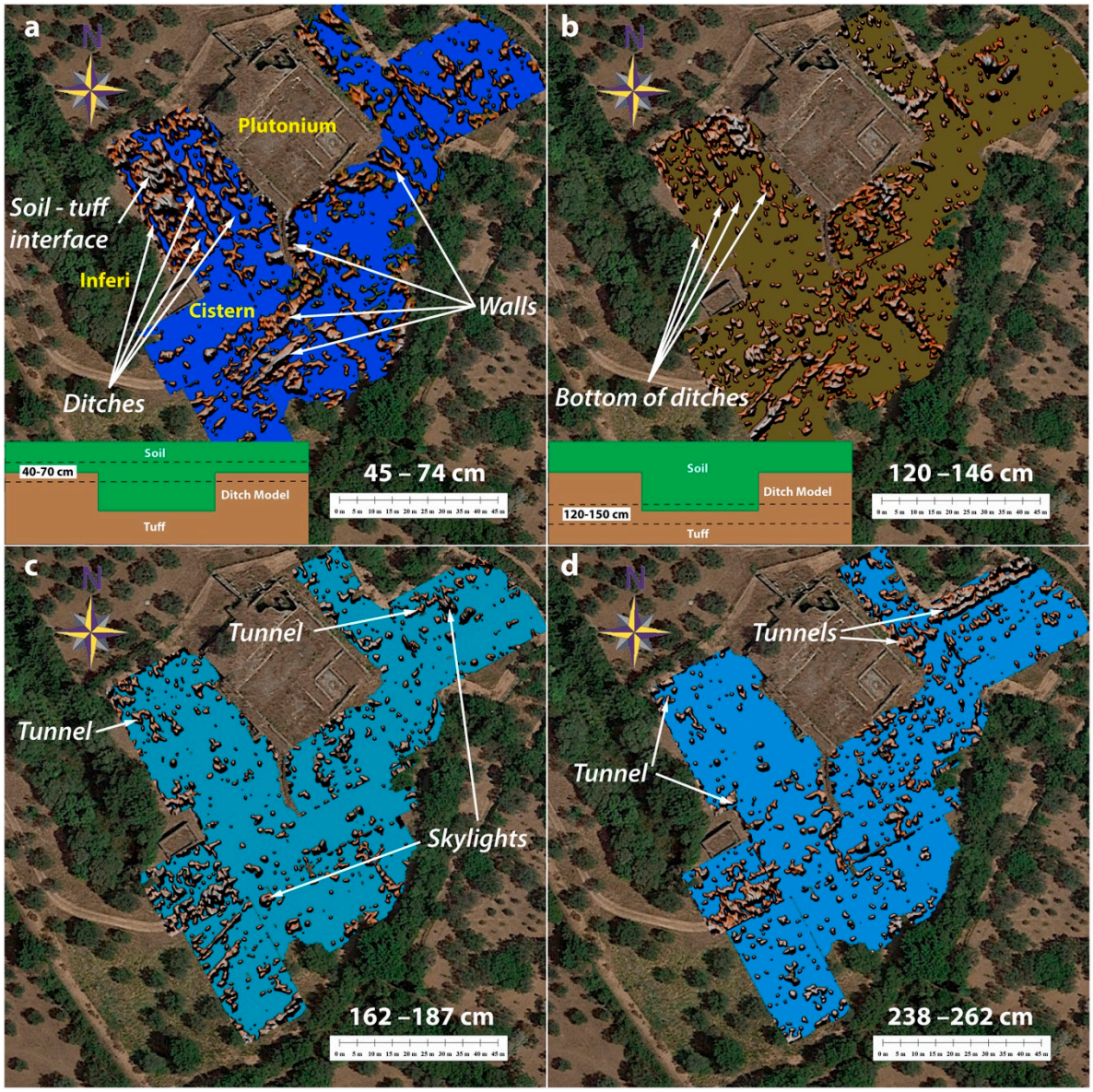

Figure 11. GPR amplitude maps for the depth intervals : (**a**) 45–74 cm (12–20 ns); (**b**) 120–146 cm (33–41 ns); (**c**) 162–187 cm (47–55 ns); (**d**) 238 – 262 cm (72–80 ns).

Both the 45–74 cm and 120–146 cm amplitude slices show the presence of structures that can be interpreted as walls [12], but an analysis of these features goes beyond the scope of this paper. The next 162–187 cm and 238–262 cm depth slices (Figure 11c–d) show the first evidence of structures that can be interpreted as tunnels and skylights. This interpretation will be discussed in the next section.

The magnetic field intensity grid obtained by the procedure described in the previous section was used to create a magnetic anomaly grid (Figure 12a) according to the method developed by [19]. In particular, the magnetic anomalies ΔT were calculated by subtraction of a 3th degree polynomial:

$$\Delta T(x,y;N) = T(x,y) - \sum_{n+m\le N} a_n b_m x^n y^m \quad (3)$$

where $T(x,y)$ are observed total field intensities, $N = 3$ is the polynomial degree of the reference field, and the coefficients a_n and b_m were calculated by statistical regression on the observed data.

Preprints (www.preprints.org) | NOT PEER-REVIEWED | Posted: 15 May 2019 doi:10.20944/preprints201905.0193.v1

Peer-reviewed version available at Remote Sens. 2019, 11, 1739; doi:10.3390/rs11151739

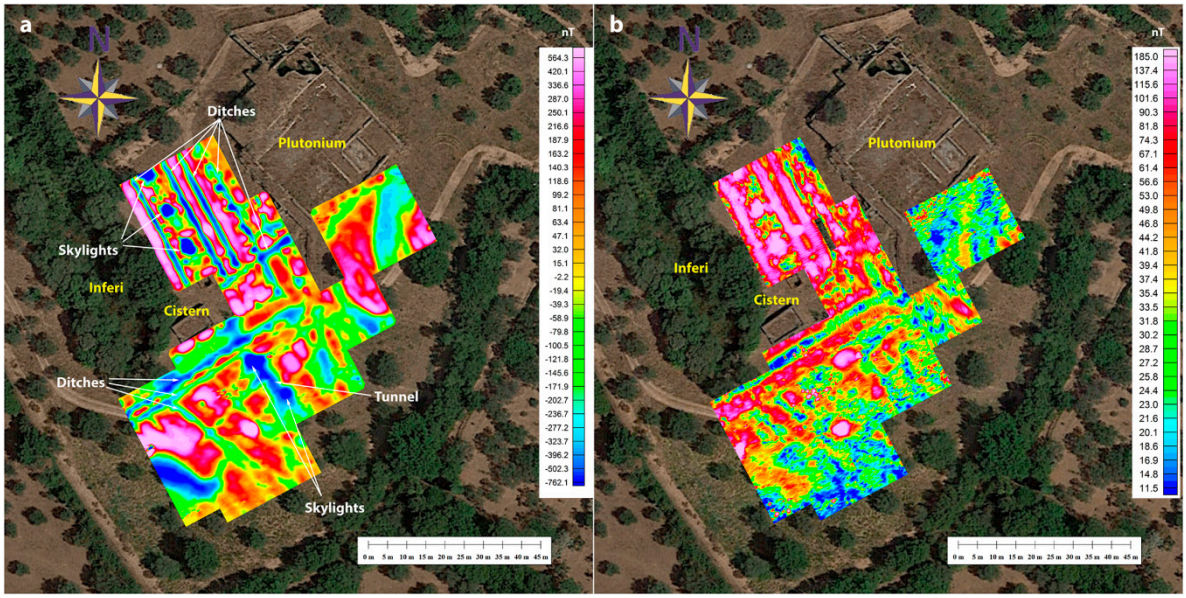

Figure 12. (**a**) The magnetic anomaly map of the Plutonium-Inferi complex; (**b**) Uncertainty grid.

Figure 12a shows that the magnetic anomalies observed in the Plutonium–Inferi area have very strong intensity. They are mostly due to air–filled and soil–filled cavities embedded in the highly magnetized bedrock. In particular, the strong circular negative anomalies visible in the map are the magnetic expression of the buried skylights observed on the GPR amplitude slices (Figure 11c–d), while the narrow linear negative anomalies reveal the presence of the ditches excavated in the tuff layer (Figure 11a–b). Differently from the maps in Figure 11, the unique visual evidence of tunnels in the magnetic anomalies consists into a small 20 m stripe of negative amplitudes aligned with the sequence of skylights (Figure 12a).

The uncertainty ε associated with the magnetic anomaly map of Figure 12a is shown in Figure 12b. It was obtained by the following expression [19,20]:

$$\varepsilon(x,y) = \varepsilon_p^2 \left|\nabla T\right| / 2^{1/3} + \varepsilon_0 \quad (4)$$

where $\left|\nabla T\right|$ is the analytic signal of the observed total field intensities, ε_P is the maximum estimated positioning error, and ε_0 is the background uncertainty associated with the statistical regression of the observed total field intensities to a polynomial surface [19]. On the basis of the field conditions, we estimated a maximum positioning error ε_P = 0.15 m, while the regression uncertainty resulted to be ε_0 = 5.29 nT. Figure 12b shows that the highest uncertainty values are found where the magnitude of the anomalies exceeds 1000 nT. An estimate of the uncertainty associated with the total field observations is necessary for the modelling of the magnetic sources (see below) to avoid overfitting of magnetic anomalies that have been calculated on the basis of a magnetization model to anomalies that are associated with observed total field intensities at a level of accuracy exceeding the actual uncertainty.

We also generated the radially averaged power spectrum [21] of the magnetic anomaly grid, with the primary objective of checking that the ensemble with the highest slope had a depth compatible with the maximum expected depths of the archaeological features [19,20,21]. However, this kind of analysis also provides a quantitative estimate of the average depths associated with the statistical ensembles that constitute the magnetic sources, which will be used in the subsequent procedure of forward modelling. The radially averaged power spectrum of Figure 13 shows the existence of four ensambles at different depths, which are in perfect agreement with the observed archaeological features in the Plutonium–Inferi area. The deepest set of sources can be found at depths exceeding 2.6 m and is most probably due to the presence of tunnels, while ditches dug at the surface of the tuff could be represented by the ensamble at ~1 m (Figure 13). Finally, walls and other

remains of archaeological features that are present at shallower depths (< 0.5 m) are represented by the two ensambles at 0.42 m and 0.26 m (Figure 13).

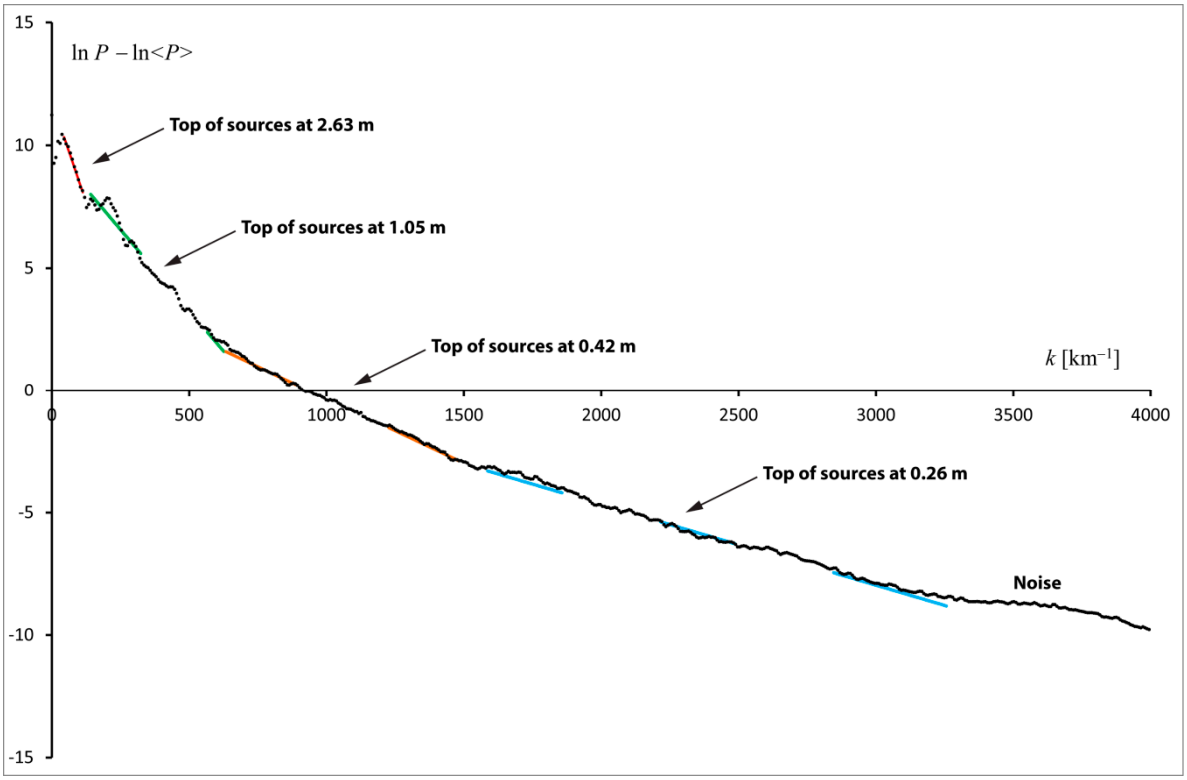

Figure 13. Radially averaged power spectrum of the magnetic anomalies in Figure 12a.

We performed a quantitative modelling of the magnetic anomalies [19,20], with the objective of assigning precise locations to tunnels and ditches but excluding from the model the much smaller signal associated with walls and other shallow features. As mentioned above, Hadrian's Villa lies on a substratum composed by an ignimbrite tuff massive deposit with very high magnetic susceptibility χ and strong NRM. In this area, the tuff is also covered by a ~0.5 m layer of very magnetic soil with susceptibility $\chi_0 = 9500\times10^{-6}$ SI units. The magnetization model shown in Figure 14 does not include archaeological features buried in this topsoil layer, thereby the fit between calculated and observed anomalies is rather coarse, although it explains most of the high–amplitude anomalies observed in this area. These two layers were modelled as slabs underneath the whole area at depths 0.5–5 m and 0–0.5 m respectively. To model empty tunnels and skylights in the tuff, we used rectangular prisms and cylinders, respectively, embedded in the tuff unit and with opposite magnetization parameters: $M_R = -4.82$ A m^{-1}, $D = 4.1°$, $I = 72.8°$, $\chi = -18127\times10^{-6}$ SI units. Similarly, to create a model of soil–filled ditches carved in the tuff, we defined vertical prisms that overlapped the uppermost part of the tuff layer with opposite NRM and susceptibility $\chi = \chi_0 - 18127\times10^{-6}$ SI units $= -8627\times10^{-6}$ SI units.

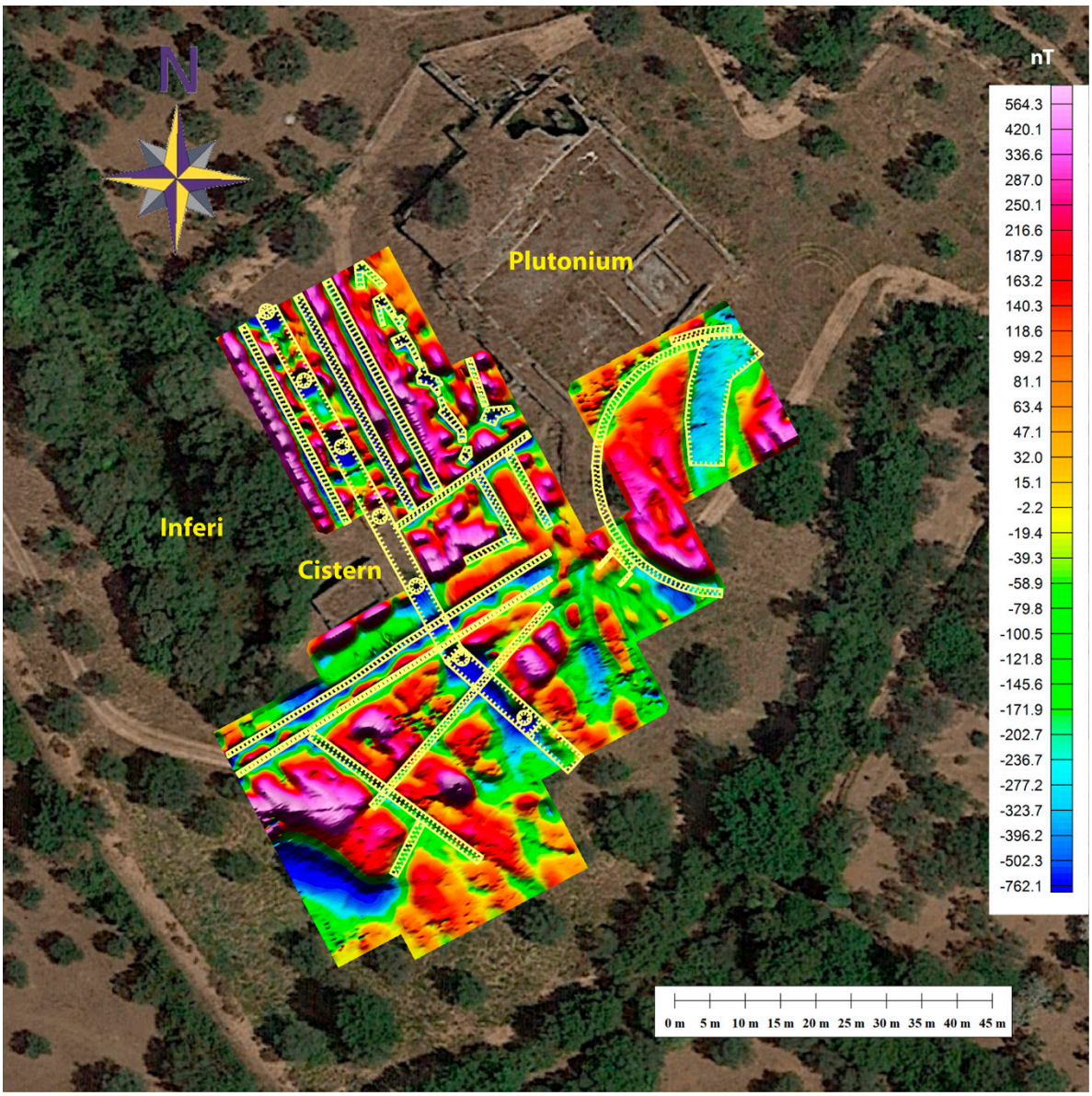

Figure 14. Magnetization model (yellow lines with barbs) of the tunnels, skylights and ditches detected in the Plutonium-Inferi area on a shaded magnetic anomaly map.

4. Discussion

The data presented in the previous section allowed us to draw a realistic layout of the tunnel network beneath the Plutonium–Inferi area. We used a computer–assisted procedure of forward modelling to generate a magnetization model that explained the observed anomalies in the western portion of the complex. An example of the accuracy of the magnetization model in Figure 14 in explaining the observed anomalies is illustrated in Figure 15. The very good fit between observed and theoretical anomalies in the two profiles suggests that the voids and soil–filled structures in the tuff are responsible for most of the magnetic signal in this area, while the walls and other artifacts embedded in the topsoil account only for a minor contribution to the observed data.

The magnetization distribution shown in Figure 14 was constrained and complemented by GPR and electric resistivity data, because of the intrinsic ambiguity of potential field data modelling. A meaningful example of the data integration procedure is illustrated in Figure 16, which shows a correlation between the three data sources. The GPR profile of Figure 16 shows a large hyperbole at 7 m offset, generated by a metallic lid covering the skylight [6]. The presence of a 5 m large tunnel flanking the Inferi (Figure 3) is confirmed by the very high resistivity region (in brown) on the electric resistivity tomography (ERT) profile, while the ditches carved at the top of the tuff are

revealed by the low resistivity regions (in blue), by the interrupted radar reflections of the soil–tuff interface, and by the displaced reflections associated with their bottom surface. Finally, the GPR profile also shows the bottom of a 180 cm high void space (20–32 ns) above the soil that partially fills the tunnel .

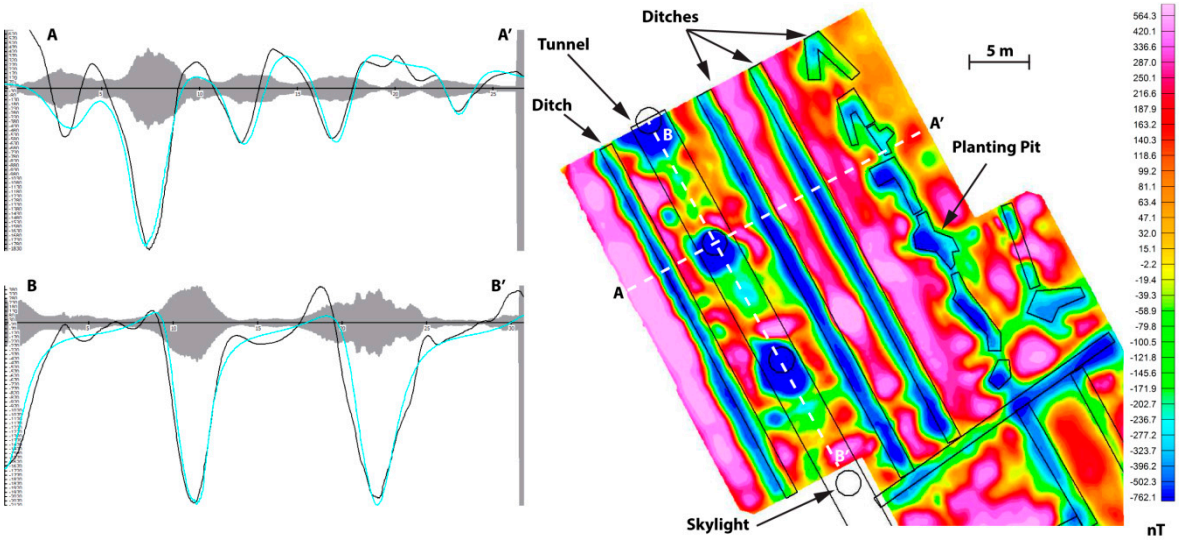

Figure 15. Magnetic profiles across the ditches, skylights, and the main tunnel of areas M15, M16, and M18 of Figure 7 (shapes bounded by black lines). The two profiles show observed and calculated anomalies as black and blue lines, respectively, while the grey area shows the local uncertainty.

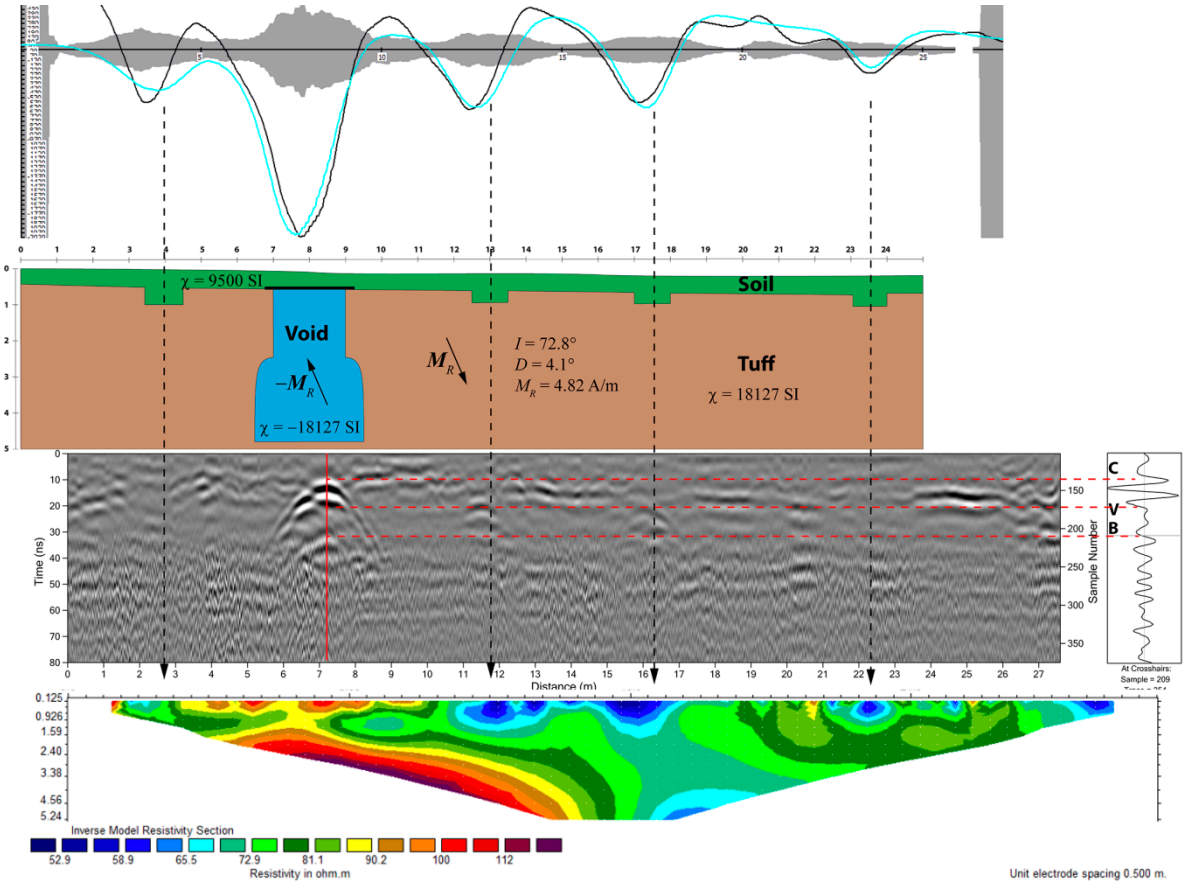

Figure 16. Correlation chart between magnetic, radar, and resistivity data showing ditches, skylights, and the main tunnel in areas M15, M16, and M18 of Figure 7. From top to bottom: magnetic profile along the trace A–A' of Figure 15, conceptual magnetization model, radar profile, and projected electric resistivity profile. C = cover wavelet; V = void top wavelet; B = void bottom wavelet. The metallic cover of the skylight is shown in black.

The magnetization model in Figures 15 and 16 does not necessarily provide a complete representation of the underground structures. For example, some ERT and GPR profiles parallel to the one shown in Figure 16 suggest the presence of a narrow tunnel below the irregular ditch running parallel to the Plutonium. Further surveys are necessary to confirm the existence of such deep structure. Instead, the pattern of ditches illustrated in Figure 15 provides a very good representation of the system of irrigation ducts and planting pits described by [22] and indicates the presence of a garden surrounding the Plutonium.

The tunnel crossing areas M15, M16, and M18 (Figure 14) corresponds to the main Strada Carrabile [14] (see Figure 3). This important 5 m large underground pathway continues in SSE direction towards areas M20–M22, where it reaches a shallower depth generating a strong linear negative magnetic anomaly, clearly visible along the skylights alignment (Figure 14). Figure 17 shows radar and ERT profiles supporting this magnetization pattern. Beyond the modern fence that surronds the archaeological park, the Strada Carrabile is linked southwards to a large four–sided system of tunnels known as the "Grande Trapezio" (Figure 3) [6].

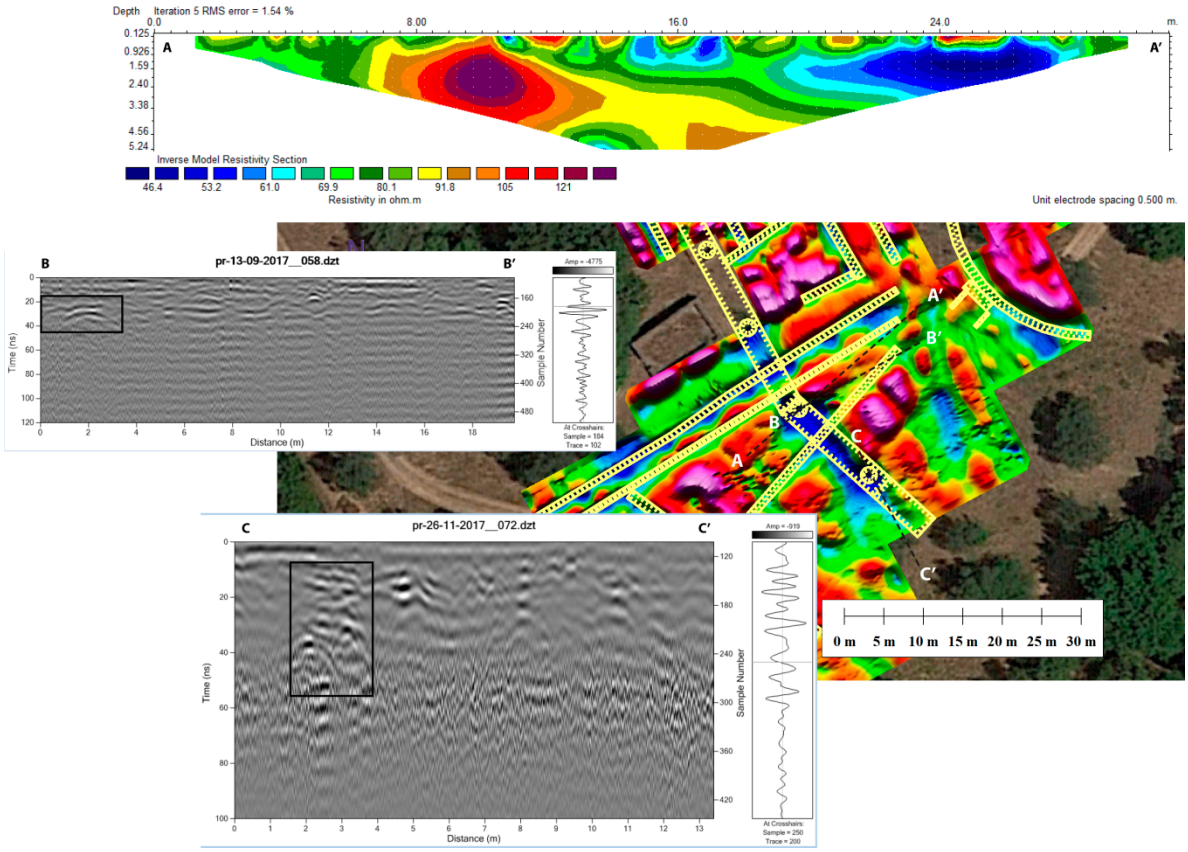

Figure 17. ERT and GPR evidence of the main tunnel and skylights in area M22 of Figure 7.

Two important findings in this sector were: 1. the identification on a series of radar profiles of an entrance to the main tunnel (Figure 18), and 2. the detection on three ERT profiles of a deep transversal tunnel running below the Strada Carrabile (Figure 19). The profiles in Figure 18 show clear evidence of two retaining walls flanking a downgoing, 1.7 m large, stairway or ramp orthogonal to the Strada Carrabile, similar to the one described by [10] for the Accademia sector. The ERT profile of Figure 19 shows a very high resistivity region that can be interpreted as a tunnel having the ceiling at ~4.5 m depth. Such a deepness can explain why the segment of Strada Carrabile located in area M22 raises towards the surface. In fact, it is likely that the deep transversal tunnel was built at an earlier time, possibly an aqueduct of Republican age [6], preceding the construction of Hadrian's Villa.

Preprints (www.preprints.org) | NOT PEER-REVIEWED | Posted: 15 May 2019 doi:10.20944/preprints201905.0193.v1

Peer-reviewed version available at Remote Sens. 2019, 11, 1739; doi:10.3390/rs11151739

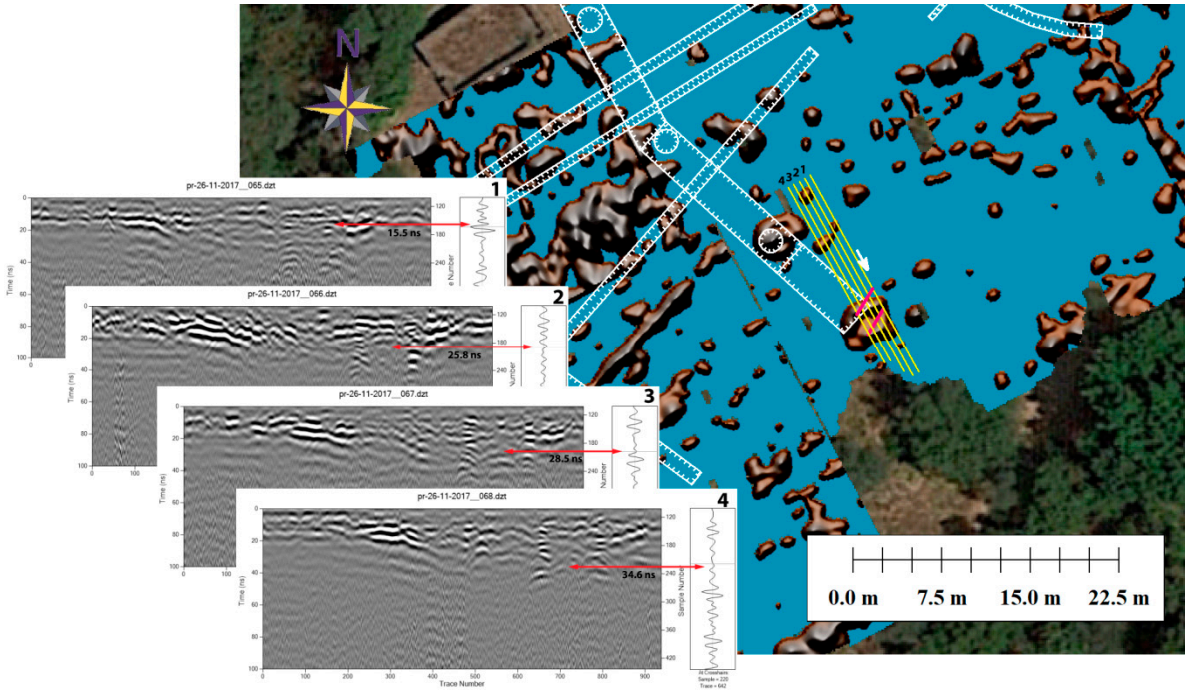

Figure 18. GPR evidence of a stairway entrance to the main tunnel. The existence of two retaining walls is evident on four radar profiles, which also show steps or a ramp at increasing depth. The stairway location is indicated by the parallel red lines on the background 162–187 cm GPR amplitude slice (Figure 11c).

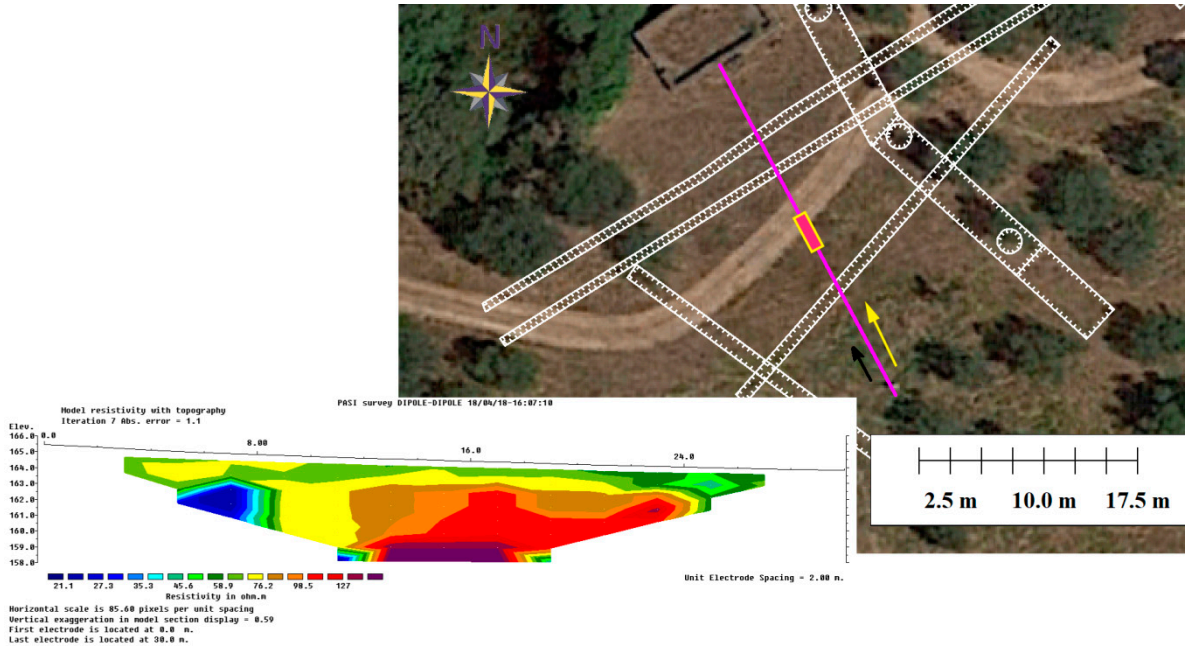

Figure 19. ERT evidence of a large deep transversal tunnel.

The eastern portion of the Plutonium–Inferi complex has not been investigated by magnetic methods due to the presence of fences. However, both GPR and electric resistivity data revealed interesting features of this sector. The ERT and GPR profiles of Figure 20 show evidence of a couple of tunnels in the direction of the northeastern slope, which could represent a way out from the villa towards the ancient Via Tiburtina. The radar profiles also show the presence of a skylight and a well filled by a jumbled assemblage of stones. The two tunnels had never been documented in previous maps. Figure 20 also shows an ERT profile with evidence of cavities flanking the eastern wall of the Plutonium, which suggests that the two tunnels in this area are linked to the Plutonium.

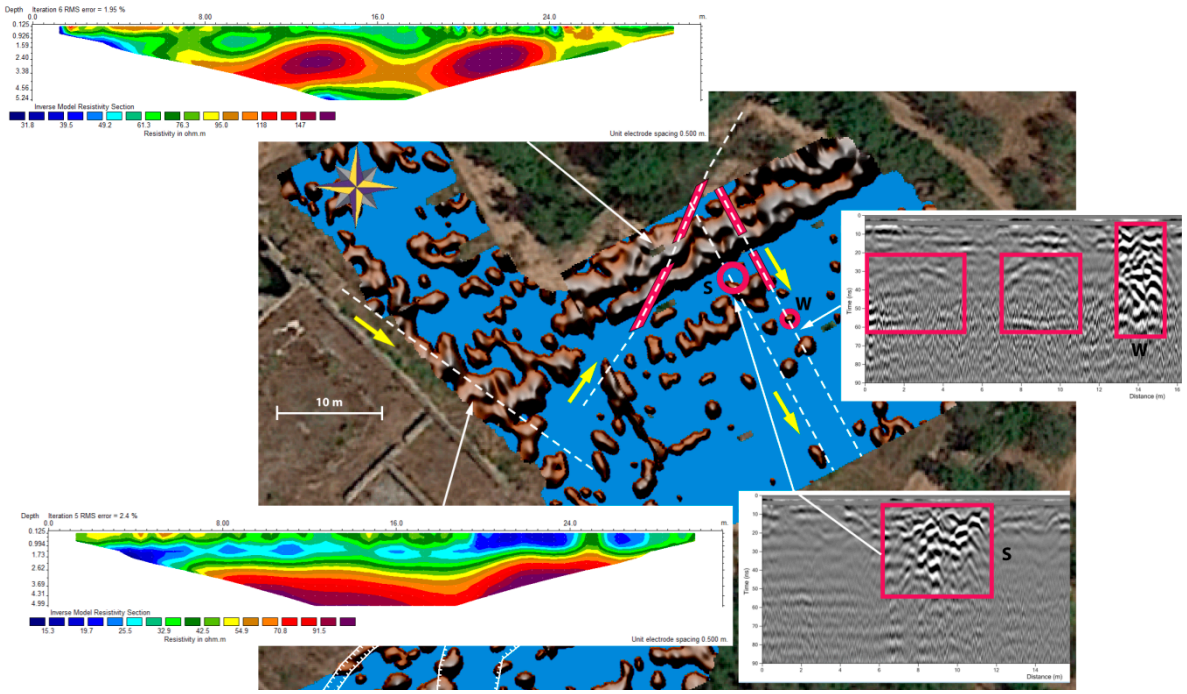

Figure 20. ERT and GPR evidence of a couple transversal tunnels linking the Plutonium to the northwestern slope. W is interpreted as a well, S is a skylight.

The map in Figure 21 combines the results presented so far, based on magnetic field modelling and the integration of radar and resistivity data. In addition to the structures discussed above, it shows a portion of a large ditch having circular shape and 32 m diameter, excavated at the soil-tuff interface. There is some archaeological evidence that this structure served to accumulate and distribute water, as it is confirmed by the finding of lead pipes during the recent excavations [12]. Together with the evidence of a garden, the presence of this structure and possibly that of a large pool within the circular area point to a reconstruction of the Plutonium–Inferi complex that included a monumental primary entrance to the Plutonium [12].

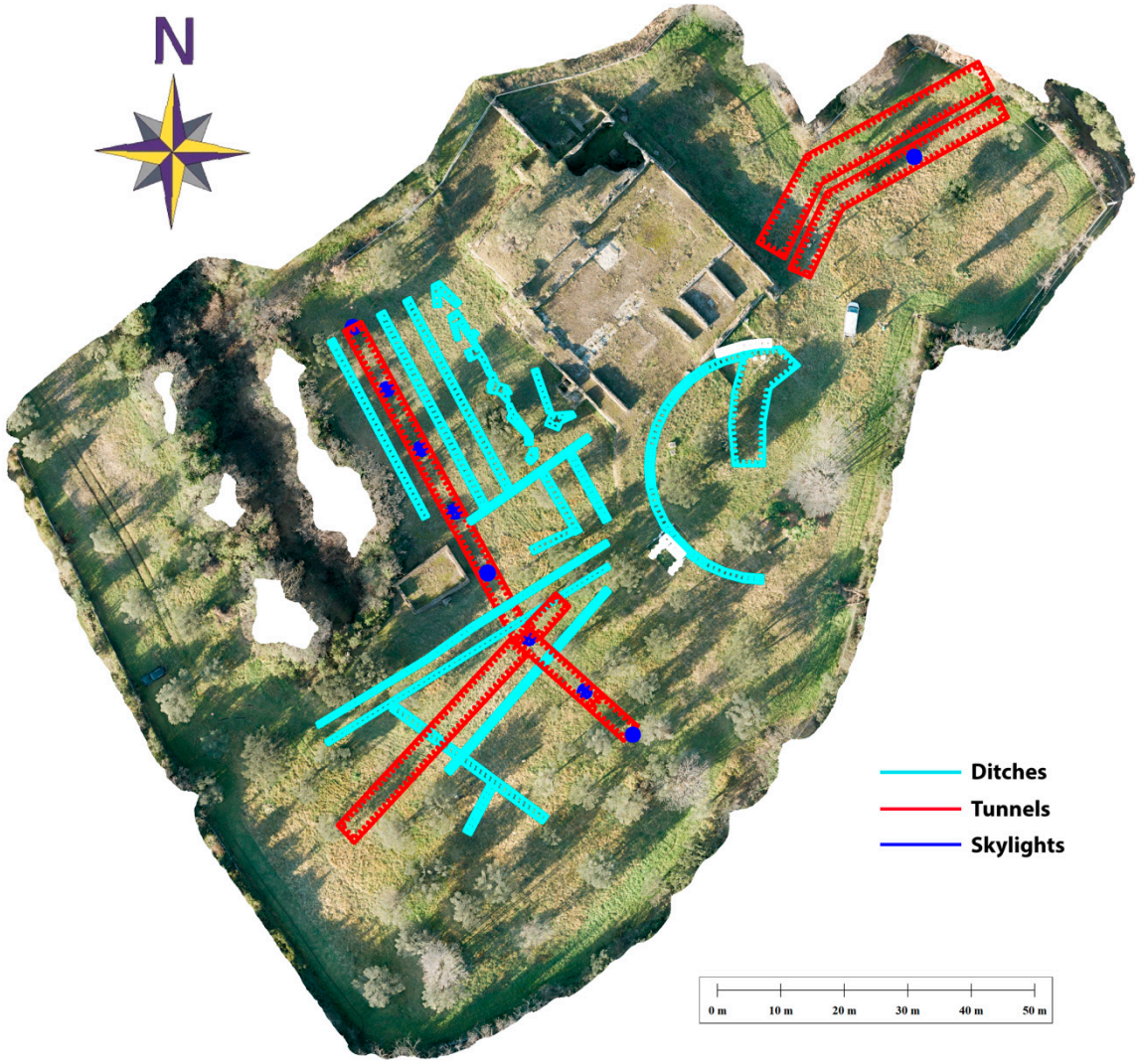

Figure 21. Final model for the tunnel network in the Plutium–Inferi area. Ditches are also displayed. Excavated walls are displayed in white [12].

5. Conclusions

In this paper, we have presented a model of the tunnels running beneath the Plutonium–Inferi area and a description of buried structures that were presumably part of a garden. The latter features consist into a system of ditches that were carved on the top of the tuff. The proposed pattern of buried structures is based on the forward modelling of magnetic anomalies, supported by GPR amplitude slices and the analysis of individual GPR and ERT profiles. In addition to the primary goal of delineating the precise location of known tunnels across the Plutonium–Inferi area, we found evidence of: *a*) an entrance to the main underground tunnel; *b*) a pair of previously unknown parallel tunnels in the eastern sector, which probably represent a way out from the villa towards the Via Tiburtina, and *c*) a previously unknown deep transversal tunnel in the western sector, probably an aqueduct of Republican age.

Author Contributions: Conceptualization of the methodology, design of the field experiments, design of the modelling software, formal analysis of magnetic and GPR data, and integration of the various sources of data, A.G. and A.S.; interpretation of radar profiles, A.G. and L.C.; acquisition, treatment, and formal analysis of paleomagnetic data, L.V. and A.G.; acquisition and formal analysis of electric resistivity data, L.T. and P.B.; mineralogical analysis of rock samples, E.S.; acquisition and formal analysis of aerial photogrammetry data, P.B.; GPS data acquisition and design of the field survey geometry, A.S., P.P.P., and A.G.; geological data acquisition and analysis, P.P.P. and E.S.; magnetic and GPR data acquisition, A.G., A.S., P.P.P., L.T., and E.S.;

original draft preparation, A.G.; review and editing, A.S., M.M., L.T., E.S., L.V., and L.C.; project supervision, A.S.; project coordination, M.E.G.

Funding: This research was funded by the Università degli Studi di Camerino, grants FAR Schettino 2016–2018 and FAR Pierantoni 2016–2018, and by the University of Oxford, Eugene Ludwig Fund, New College.

Acknowledgments: The authors are grateful to the Director of the Villa Adriana and Villa d'Este, Dr. Andrea Bruciati, for kindly allowing to survey the archaeological area and to Drs. Benedetta Adembri and Sabrina Pietrobono for facilitating the research on site. We are also grateful to Francesco Ferruti and the students that helped us in the data acquisition. Finally, we thank Alessandro Bertani for his help in the acquisition and formal analysis of aerial photogrammetry data.

Conflicts of Interest: The authors declare no conflict of interest. The funders had no role in the design of the study; in the collection, analyses, or interpretation of data; in the writing of the manuscript, or in the decision to publish the results.

References

1. Funiciello, R.; Giordano, G.; De Rita, D. The Albano maar lake (Colli Albani Volcano, Italy): recent volcanic activity and evidence of pre-Roman Age catastrophic lahar events.*J. Volcanol. Geotherm. Res.* **2003**, *123*, 43-61.
2. Giordano, G.; De Benedetti, A.A.; Diana, A.; Diano, G.; Gaudioso, F.; Marasco, F.; Miceli, M.; Mollo, S.; Cas, R.A.F.; Funiciello, R. The Colli Albani mafic caldera (Roma, Italy): Stratigraphy, structure and petrology. *J. Volcanol. Geotherm. Res.* **2006**, *155*, 49-80.
3. Soligo, M.; Tuccimei, P. Geochronology of Colli Albani volcano. In *The Colli Albani Volcano*; Funiciello, R., Giordano, G. Eds.; Special Publications of IAVCEI, 3. The Geological Society of London, London, **2010**; pp. 154-196.
4. Vinkler, A.P.; Cashman, K.; Giordano, G., Groppelli, G. Evolution of the mafic Villa Senni caldera-forming eruption at Colli Albani volcano, Italy, indicated by textural analysis of juvenile fragments. *J. Volcanol. Geotherm. Res.* **2012**, *235-236*, 37-54.
5. Watkins, S.D.; Giordano, G.; Cas, R.A.F.; De Rita, D. Emplacement processes of the mafic Villa Senni Eruption Unit (VSEU) ignimbrite succession, Colli Albani volcano, Italy. *J. Volcanol. Geotherm. Res.* **2002**, *118*, 173-203.
6. Salza Prina Ricotti E. Criptoportici e Gallerie sotterranee di Villa Adriana nella loro tipologia e nelle loro funzioni. *Publications de l'École Française de Rome* **1973**,*14(1)*, 219-59.
7. Ligorio, P. Codice Vaticano latino 5295,*Trattato delle Antichità di Tivoli et della Villa Hadriana fatto da Pyrrho Ligorio Patritio 72 Napoletano et dedicato all'Ill.mo Cardinal di Ferrara*. Biblioteca Apostolica Vaticana, Cod. Vat. Lat. 5295 fol. 1r - 32 v.
8. Contini, F. *Hadriani Caesaris immanem in agro tiburtino villam*, Roma, Italy, tav. VIII, **1668**.
9. Penna, A.; *Viaggio pittorico della Villa Adriana composto di vedute disegnate dal vero ed incise da Agostino Penna con una breve descrizione di ciascun monumento*; tipografia Pietro Aureli, Roma,**1836**.
10. De Franceschini, M.; A. M. Marras. New discoveries with geophysics in the Accademia of Hadrian's Villa near Tivoli (Rome) *Advances in Geosciences* **2010**, *24*, 2.
11. Hay, S. The Plutonium at Hadrian's Villa: Geophysical Survey Report **2016**, 1-29.
12. Gorrini, M.E.; Melfi, M.; Montali, G.; Schettino, A. Il progetto Plutonium di Villa Adriana: Prime considerazioni a margine del nuovo rilievo e prospettive di ricerca. In G.E. Cinque et al. eds., Adventus Hadriani, Convegno internazionale di studi, Roma-Tivoli 4-7 luglio 2018, in press.
13. Verdiani, G. Cryptoporticus, La rete delle strade diventa sotterranea a Villa Adriana, Tivoli, *Firenze Architettura* **2017**, *21*(1), 162-169. DOI 10.13128/FiAr-21071.
14. Placidi, M.; Fresi, V. Tivoli, Villa Adriana, Strada sotterranea cd "Strada Carrabile", Campagna di studio 2007-2008, breve sintesi dei risultati. *The Journal of Fasti Online* **2010**, *190*, 1-6.
15. Colvin, H. *Architecture and the After-Life*; Yale University Press: 47 Bedford Square London WC1B 3DP, U.K., **1992**.
16. Solheid, P.A. Mössbauer revisited. *The IRM Quaterly*, **1998**, *8*(3), 1-6.
17. Loke MH, Barker RD. Least-squares deconvolution of apparent resistivity pseudosections. *Geophysics* **1995**, *60*(6),1682-90.

18. Conyers, L. B. *Ground-penetrating radar and magnetometry for buried landscape analysis*; Springer, **2018**.
19. Schettino, A., Ghezzi, A. and Pierantoni, P.P. Magnetic field modelling and analysis of uncertainty in archaeological geophysics. *Archaeological Prospection* **2018,** doi:10.1002/arp.1729
20. Ghezzi A., Schettino A., Tassi L. and Pierantoni P.P. Magnetic modelling and error assessment in archaeological geophysics: The case study of Urbs Salvia, central Italy. Annals of Geophysics 2018, 61, doi: 10.4401/ag-7799.
21. Spector A. and Grant F.S. Statistical models for interpreting aeromagnetic data. *Geophysics* **1970**, *35*, 293-302.
22. Jashemski W.F. and Salza Prina Ricotti E. Preliminary excavations in the gardens of Hadrian's Villa: the Canopus area and the Piazza d'Oro. *American J. of Archaeology* **1992**, *96*, 579–597.